



Numerical Heat Transfer, Part A: Applications

An International Journal of Computation and Methodology

ISSN: 1040-7782 (Print) 1521-0634 (Online) Journal homepage: www.tandfonline.com/journals/unht20

Numerical simulation of solar wind energy towers

L. Hijazi, I. A. Fayssal, M. Darwish & F. Moukalled

To cite this article: L. Hijazi, I. A. Fayssal, M. Darwish & F. Moukalled (2017) Numerical simulation of solar wind energy towers, Numerical Heat Transfer, Part A: Applications, 72:10, 780-805, DOI: [10.1080/10407782.2017.1400344](https://doi.org/10.1080/10407782.2017.1400344)

To link to this article: <https://doi.org/10.1080/10407782.2017.1400344>



Published online: 27 Nov 2017.



Submit your article to this journal [↗](#)



Article views: 182



View related articles [↗](#)



View Crossmark data [↗](#)



Numerical simulation of solar wind energy towers

L. Hijazi, I. A. Fayssal, M. Darwish, and F. Moukalled

Department of Mechanical Engineering, American University of Beirut, Beirut, Lebanon

ABSTRACT

A numerical investigation is conducted to study the performance of solar wind energy towers. The two-phase flow of air and water droplets in the tower is modeled following an Euler–Lagrange approach with air representing the continuous phase and water droplets the discrete phase. Results demonstrate that energy towers perform best in hot and dry environments. Water injection at the inlet to a tower increases the strength of the downdraft current with the rate of increase diminishing as the flow at exit approaches saturation. At a given water injection rate and tower diameter the downdraft strength increases as the height increases, while it is independent of the diameter at constant height. Energy analysis shows that for towers of low height the cost of electricity is expensive and commercially unfeasible, while it is cheap for towers of heights higher than 100 m.

ARTICLE HISTORY

Received 16 August 2017

Accepted 26 October 2017

Introduction

A downdraft energy tower is a power plant that produces electricity in hot and dry climates. It is composed of a hollow cylinder, a spraying system placed at the top of the tower, and a pumping station and turbines located at the bottom of the arrangement. Water is sprayed across the inlet cross section of the tower and as droplets move with the air, evaporation takes place. Thus, the air inside becomes denser and cooler than the ambient air creating a downdraft within the enclosed space. At the bottom of the tower, the high velocity airflow drives turbines and generates electricity. As cool air descends, dry and warmer air is sucked in from the top making the process continuous.

The concept of the energy tower was first introduced by Carlson [1] who suggested initiating a downdraft in a hollow duct by spraying water at its top and harnessing power from turbines located at its bottom. However, there were many flaws in Carlson's patent that were tackled by Zaslavsky et al. [2]. Abhinava et al. [3] studied theoretically the factors impacting the exit velocity of a 500 m tower. Their analysis revealed the importance of the tower height, negative available potential energy, precipitation loading, and maximum horizontal momentum on performance. Similarly, Bauer and Gasser [4] modeled the transient flow and power production in an energy tower by reducing the one-dimensional Euler equations for a compressible humid air gas mixture into an asymptotic system of equations, which was solved numerically.

The stream in the channel is a two-phase flow involving the gas and the droplet phases. The gas phase is multispecies composed of dry air and water vapor. The humidity ratio (i.e., the amount of water vapor per unit mass of dry air) increases as the air moves down the channel due to evaporation of the sprayed liquid water. To simulate the droplet transport and evaporation phenomenon, two routes have been followed that are denoted in the literature by the Euler–Lagrange (EL) [5–11] and the Euler–Euler (EE) [12–20] approaches. In both methods, the gas phase is represented in an Eulerian framework where the Navier–Stokes equations are solved. In the Euler–Euler approach, each

Nomenclature

<p>A_d droplet surface area (m^2)</p> <p>B_m Spalding mass transfer number</p> <p>B_T Spalding heat transfer number</p> <p>$c_{p,d}$ water droplet specific heat ($J/kg\ K$)</p> <p>C_D drag coefficient</p> <p>d_d water droplet diameter (m)</p> <p>D tower diameter (m)</p> <p>D_v diffusivity of water vapor in air (m^2/s)</p> <p>E total energy (J/kg)</p> <p>h convection heat transfer coefficient ($W/m^2\ K$)</p> <p>H tower height (m)</p> <p>h_{fg} latent heat of evaporation (J/kg)</p> <p>h_v vapor enthalpy (J/kg)</p> <p>k turbulence kinetic energy (J/kg)</p> <p>m_d droplet mass (kg)</p> <p>\dot{m}_{air} mass flow rate of the gas mixture (kg/s)</p> <p>Nu Nusselt number</p> <p>p pressure (Pa)</p> <p>Pr Prandtl number</p> <p>Q enhancement in mass flow rate</p> <p>r radial coordinate (m)</p> <p>Re_d Reynolds number based on the droplet diameter</p> <p>S_m source term in continuity and vapor mass fraction equations</p> <p>S_h source term in energy equation</p>	<p>S_x source term in x-momentum equation</p> <p>S_r source term in r-momentum equation</p> <p>Sh Sherwood number</p> <p>Sc Schmidt number</p> <p>t time (s)</p> <p>T temperature (K)</p> <p>T_{air} air temperature (K)</p> <p>T_d droplet temperature (K)</p> <p>T_{ref} reference temperature for enthalpy (K)</p> <p>v_d droplet velocity vector</p> <p>v_x axial component of velocity (m/s)</p> <p>v_r radial component of velocity (m/s)</p> <p>\mathbf{v} velocity vector of the continuous phase</p> <p>V_{air} velocity of moist air (m/s)</p> <p>W humidity ratio (kg_{vapor}/kg_{dryair})</p> <p>x axial coordinate (m)</p> <p>x_d droplet position vector</p> <p>Y_v mass fraction of water vapor in the gas phase</p> <p style="text-align: center;">Greek symbols</p> <p>ε turbulence dissipation rate ($J/kg\ s$)</p> <p>μ, μ_t laminar and turbulent viscosity ($kg/m\ s^2$)</p> <p>λ effective thermal conductivity ($W/m\ K$)</p> <p>ρ air density (kg/m^3)</p> <p>ρ_d droplet density (kg/m^3)</p> <p>ϕ relative humidity</p>
--	---

phase is treated in an Eulerian Framework with phases treated separately, but interactively. Both the spray and gas phases are solved using the same numerical procedure with the Navier–Stokes equations extended to incorporate interphase exchange coefficients representing the transfer of mass, momentum, and energy between phases. In the Euler–Lagrange approach, droplets represent the discrete phase, while the gas represents the continuous phase. Interphase exchange terms of mass, momentum, and energy appear in the Eulerian conservation equations and these sources are obtained by alternating iterations between equations representing both phases. The advantages of the LE method over the EE method for accurately simulating the evaporation process are highlighted by Subramaniam [21].

Experimental studies have been conducted on small scale energy towers, the passive downdraft evaporative cooling (PDEC) tower. This tower is a few stories high and the produced flow is used to cool and ventilate spaces rather than to generate electricity. Work reported in Refs [22–24], used numerical simulation and adopted the LE method to predict airflows in PDEC towers. The objective of this work is to investigate the performance of solar wind energy towers. Since the cost of building an actual tower is prohibitive, a numerical approach is followed. The study differs from previously reported ones in analyzing the true performance of the tower. The considered tower is cylindrical in shape, the flow is assumed to be axisymmetric, and simulations are performed under steady state conditions. The conservation equations governing the flow, mass transfer, and heat transfer fields are solved in a LE framework using the FLUENT software package. The air mass flow rate produced in comparison with the amount of sprayed water is investigated. The predicted conditions at the exit of the tower, including velocity, temperature, density, and relative humidity under various ambient conditions and spray characteristics are reported. From these predicted conditions, the power that can be extracted from the wind stream exiting the tower is estimated.

In the remainder of this article, the Euler–Lagrange approach, the physical situation, and the conservation equations governing the flow, heat, and mass transfer fields are first reviewed. This is followed by a description of the adopted numerical method, the developed user-defined function

(UDF), and boundary conditions. Then the suggested model is validated by comparing its predictions with available measurements obtained from a small scale PDEC tower. The paper proceeds with a parametric study showing the effects of the injection rate, ambient conditions, droplet diameter, and tower height and diameter on tower performance. The article ends with a section on energy analysis showing the electric power that can be produced and its cost.

Euler–Lagrange approach

The flow in the current study is composed of two phases denoted by the discrete and the continuous phase. The discrete phase is composed of droplets of liquid water while the continuous/gas phase is made up of two species, which are air and water vapor. In the Euler–Lagrange approach [5–11], the gas phase is predicted by solving its transport equation in an Eulerian reference frame while the discrete dispersed phase is solved in a Lagrangian reference frame. Interphase exchange terms appear as sources in the time averaged Navier–Stokes equations in the continuous phase, which express the exchange of mass, momentum, and energy with the discrete phase. The fully turbulent flow is assumed to be steady and axisymmetric and the spray of water is dilute with spherical droplets. Water evaporation is assumed to be slow, convection–diffusion controlled, and of constant latent heat.

Physical situation and conservation equations

The physical situation can be described by referring to Figure 1. As air enters the domain (the continuous gas phase), liquid water is sprayed in the form of droplets into the flowing stream. The droplets moving with the air evaporate and decrease in size. Two sets of mass, momentum, and energy equations are required to predict the flow, heat, and mass transfer fields. One set for the continuous gas phase written in an Eulerian reference frame and a second set for the discrete droplet phase expressed in a Lagrangian reference frame. An additional equation to track the mass fraction of

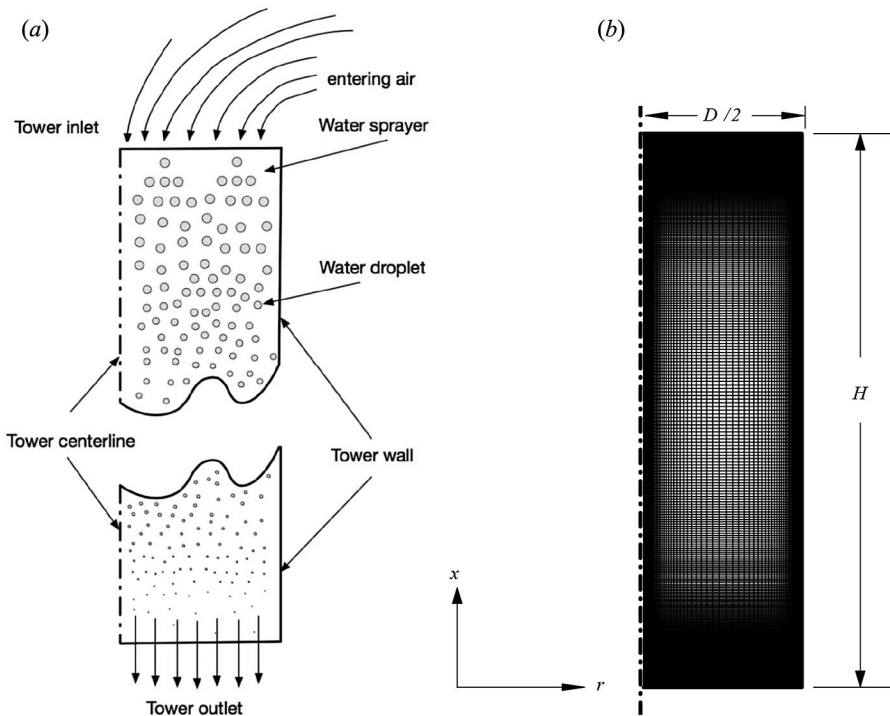


Figure 1. (a) Physical and (b) computational domain for the solar wind energy tower.

water vapor is also needed. Moreover, as the flow is assumed to be turbulent, additional equations to compute the Reynolds stresses are necessary. In this work the standard $k - \varepsilon$ model [25] is adopted for the gas phase, while for the discrete phase the dispersion of droplets due to turbulence is accounted for using the stochastic tracking approach based on the integral time scale. Neglecting interaction between droplets, the flow field is described by the transport equations presented next.

Continuous phase equations

In the continuous gas phase, the equations representing the conservation of mass, momentum, energy, and mass fraction of the water vapor in axisymmetric coordinates are solved. To quantify turbulence, the k and ε equations of the Standard $k - \varepsilon$ turbulence model are appended to the conservation equations, leading to the following extended system of Reynolds-averaged Navier–Stokes equations:

$$\frac{\partial \rho}{\partial t} + \frac{\partial}{\partial x}(\rho v_x) + \frac{\partial}{\partial r}(\rho v_r) + \frac{\rho v_r}{r} = S_m \quad (1)$$

$$\begin{aligned} \frac{\partial}{\partial t}(\rho v_x) + \frac{1}{r} \frac{\partial}{\partial x}(r \rho v_x v_x) + \frac{1}{r} \frac{\partial}{\partial r}(r \rho v_r v_x) = - \frac{\partial p}{\partial x} \\ + \frac{1}{r} \frac{\partial}{\partial x} \left[r \mu \left(2 \frac{\partial v_x}{\partial x} - \frac{2}{3} \left(\frac{\partial v_x}{\partial x} + \frac{\partial v_r}{\partial r} + \frac{v_r}{r} \right) \right) \right] + \frac{1}{r} \frac{\partial}{\partial r} \left[r \mu \left(\frac{\partial v_x}{\partial r} + \frac{\partial v_r}{\partial x} \right) \right] + S_x \end{aligned} \quad (2)$$

$$\begin{aligned} \frac{\partial}{\partial t}(\rho v_r) + \frac{1}{r} \frac{\partial}{\partial x}(r \rho v_x v_r) + \frac{1}{r} \frac{\partial}{\partial r}(r \rho v_r v_r) = - \frac{\partial p}{\partial r} + \frac{1}{r} \frac{\partial}{\partial x} \left[r \mu \left(\frac{\partial v_r}{\partial x} + \frac{\partial v_x}{\partial r} \right) \right] \\ + \frac{1}{r} \frac{\partial}{\partial r} \left[r \mu \left(2 \frac{\partial v_r}{\partial r} - \frac{2}{3} \left(\frac{\partial v_x}{\partial x} + \frac{\partial v_r}{\partial r} + \frac{v_r}{r} \right) \right) \right] - 2 \mu \frac{v_r}{r^2} + \frac{2}{3} \frac{\mu}{r} \left(\frac{\partial v_x}{\partial x} + \frac{\partial v_r}{\partial r} + \frac{v_r}{r} \right) + S_r \end{aligned} \quad (3)$$

$$\begin{aligned} \frac{\partial}{\partial t}(\rho E) + \frac{\partial}{\partial x}[v_x(\rho E + p)] + \frac{1}{r} \frac{\partial}{\partial r}[r v_r(\rho E + p)] = \frac{\partial}{\partial x} \left(\lambda \frac{\partial T}{\partial x} \right) + \frac{1}{r} \frac{\partial}{\partial r} \left(r \lambda \frac{\partial T}{\partial r} \right) \\ - \left[\frac{\partial}{\partial x} \left(h_v \rho D_v \frac{\partial Y_v}{\partial x} \right) + \frac{1}{r} \frac{\partial}{\partial r} \left(r h_v \rho D_v \frac{\partial Y_v}{\partial r} \right) \right] + S_h \end{aligned} \quad (4)$$

$$\frac{\partial}{\partial t}(\rho Y_v) + \frac{\partial}{\partial x}(\rho v_x Y_v) + \frac{1}{r} \frac{\partial}{\partial r}(r \rho v_r Y_v) = \frac{\partial}{\partial x} \left(\rho D_v \frac{\partial Y_v}{\partial x} \right) + \frac{1}{r} \frac{\partial}{\partial r} \left(r \rho D_v \frac{\partial Y_v}{\partial r} \right) + S_m \quad (5)$$

$$\begin{aligned} \frac{\partial}{\partial t}(\rho k) + \frac{\partial}{\partial x}(\rho v_x k) + \frac{1}{r} \frac{\partial}{\partial r}(r \rho v_r k) = \frac{1}{r} \frac{\partial}{\partial r} \left(r \left(\mu + \frac{\mu_t}{\sigma_k} \right) \frac{\partial k}{\partial r} \right) \\ + \frac{\partial}{\partial x} \left(\left(\mu + \frac{\mu_t}{\sigma_k} \right) \frac{\partial k}{\partial x} \right) + G_k + G_b - \rho \varepsilon - Y_M + S_k \end{aligned} \quad (6)$$

$$\begin{aligned} \frac{\partial}{\partial t}(\rho \varepsilon) + \frac{\partial}{\partial x}(\rho v_x \varepsilon) + \frac{1}{r} \frac{\partial}{\partial r}(r \rho v_r \varepsilon) = \frac{1}{r} \frac{\partial}{\partial r} \left(r \left(\mu + \frac{\mu_t}{\sigma_\varepsilon} \right) \frac{\partial \varepsilon}{\partial r} \right) \\ + \frac{\partial}{\partial x} \left(\left(\mu + \frac{\mu_t}{\sigma_\varepsilon} \right) \frac{\partial \varepsilon}{\partial x} \right) + C_1 \frac{\varepsilon}{k} (G_k + C_3 G_b) - C_2 \rho \frac{\varepsilon^2}{k} + S_\varepsilon \end{aligned} \quad (7)$$

The source terms S_m , S_x , S_r , and S_h appearing in the continuity (Eq. 1), momentum (Eqs. 2 and 3), energy (Eq. 4), and vapor mass fraction (Eq. 5) equations represent the interphase exchange terms between the continuous and discrete phases and will be summarized in a later section. Detailed explanations can be found in ANSYS FLUENT theory guide [26].

Discrete phase equations

In the discrete phase, the trajectory, velocity, and temperature of the droplets are calculated by integrating their respective equations, written in a Lagrangian reference frame, over the discrete phase time step. These equations are given by

$$\frac{d\mathbf{x}_d}{dt} = \mathbf{v}_d \quad (8)$$

$$\frac{d\mathbf{v}_d}{dt} = F_D(\mathbf{v} - \mathbf{v}_d) + \mathbf{g} \frac{(\rho_d - \rho)}{\rho_d} + \mathbf{F} \quad (9)$$

$$m_d c_{p,d} \frac{dT_d}{dt} = hA_d(T_{\text{air}} - T_d) + \frac{dm_d}{dt} h_{fg} \quad (10)$$

The trajectory of the droplet is obtained by integrating Eq. (8) over time, while its velocity at each point along the trajectory is predicted by integrating Eq. (9) over discrete time steps. The droplet momentum equation (Eq. 9) represents a balance between inertia of the droplet (the term on the left-hand side) and the forces acting on it (the terms on the right-hand side). The first two terms on the right-hand side of Eq. (9) represent the drag and buoyancy forces. The force \mathbf{F} accounts for all other forces, which may include the virtual mass and the pressure gradient forces. These forces are important and should be added when $\rho/\rho_d \geq 0.1$. Since for the considered case $\rho/\rho_d \approx 10^{-3}$, these forces are neglected. The coefficient F_D of the drag force is computed as

$$F_D = \frac{18\mu}{\rho_d d_d^2} \frac{C_D \text{Re}_d}{24} \quad (11)$$

where the drag coefficient C_D is calculated using the relation developed by Morsi and Alexander [27] as

$$C_D = a_1 + \frac{a_2}{\text{Re}_d} + \frac{a_3}{\text{Re}_d^2} \quad (12)$$

The values of a_1 , a_2 , and a_3 depend on the droplet Reynolds number Re_d , which is computed based on the droplet diameter d_d and the relative velocity between the droplet and the surrounding air as

$$\text{Re}_d = \frac{\rho_{\text{air}} d_d |\mathbf{v}_d - \mathbf{v}_{\text{air}}|}{\mu} \quad (13)$$

The droplet temperature is predicted from Eq. (10), which relates the sensible heat change in the droplet (the term on the left-hand side) to the convective (first term on the right-hand side) and latent heat transfer (second term on the right-hand side) between the droplet and the surrounding air. The rate of evaporation is computed using the convection-diffusion mass transfer model [28, 29] as

$$\frac{dm_d}{dt} = k_c A_d \rho_{\text{air}} \text{Ln}(1 + B_m) \quad (14)$$

where k_c is the mass transfer coefficient and B_m is the Spalding mass transfer number obtained from

$$B_m = \frac{Y_{v,s} - Y_{v,\infty}}{1 - Y_{v,s}} \quad (15)$$

where $Y_{v,s}$ and $Y_{v,\infty}$ are the vapor mass fraction at the droplet surface and in the bulk gas, respectively. The mass transfer coefficient (k_c) is calculated from the Sherwood number (Sh) as [30, 31]

$$\text{Sh} = \frac{k_c d_d}{D_v} = 2. + 0.6 \text{Re}_d^{1/2} \text{Sc}^{1/3} \quad (16)$$

where Sc is the Schmidt number defined by

$$Sc = \frac{\mu}{\rho D_v} \quad (17)$$

The convection heat transfer coefficient in Eq. (10) is computed as [30, 31]

$$Nu = \frac{hd_d}{k_\infty} = \frac{\text{Ln}(1 + B_T)}{B_T} \left(2. + 0.6\text{Re}_d^{1/2} \text{Pr}^{1/3} \right) \quad (18)$$

where $\text{Pr} = \mu c_p / \lambda_{\text{air}}$ is the Prandtl number, λ_{air} is the air thermal conductivity, and B_T is the Spalding heat transfer number set equal to B_m .

The dispersion of particles due to turbulence is evaluated using a stochastic tracking model. In this approach the effects of the turbulence of the gas phase on the droplet motion is accounted for using in Eq. (9) the actual gas velocity vector \mathbf{v} , which is the sum of an average $\bar{\mathbf{v}}$ and a fluctuating \mathbf{v}' part, i.e.,

$$\mathbf{v} = \bar{\mathbf{v}} + \mathbf{v}' \quad (19)$$

Since a two-equation $k - \varepsilon$ turbulence model is used for the gas phase, the solution of the continuous phase equations allows predicting $\bar{\mathbf{v}}$. In the random walk model, the fluctuating part \mathbf{v}' is sampled by a Gaussian probability distribution function as

$$v'_x = \xi \sqrt{v_x'^2} \quad v'_r = \xi \sqrt{v_r'^2} \quad (20)$$

where ξ is a normally distributed random number, and $\sqrt{v_x'^2}$ and $\sqrt{v_r'^2}$ are the local RMS values of velocity fluctuations and are represented as

$$\sqrt{v_x'^2} = \sqrt{v_r'^2} = \sqrt{\frac{2k}{3}} \quad (21)$$

In addition, each eddy is also represented by a characteristic lifetime τ_e given by

$$\tau_e = 2T_L \quad (22)$$

where T_L is the Lagrangian time scale. For the $k - \varepsilon$ model, this time scale is approximated as

$$T_L \approx 0.15 \frac{k}{\varepsilon} \quad (23)$$

Furthermore, the particle eddy cross time is defined as

$$t_{\text{cross}} = -\tau \text{Ln} \left[1 - \frac{L_e}{\tau |\mathbf{v} - \mathbf{v}_d|} \right] \quad (24)$$

where τ_e is the droplet relaxation time, and L_e is the eddy length scale. The particle is assumed to interact with the fluid phase eddy over the eddy lifetime and the eddy crossing time. When this time is reached, a new value of the instantaneous velocity is obtained by applying a new value of ξ .

Interphase coupling

As mentioned earlier, the coupling between the continuous and discrete phases is accomplished through the source terms appearing in the various continuous phase equations.

The transfer of mass by evaporation from the discrete to the continuous phase is computed by evaluating the change in the mass of the droplet as it crosses an element using the following equation:

$$S_m = \frac{\Delta m_d}{m_{d,0}} \dot{m}_{d,0} \quad (25)$$

where $\dot{m}_{d,0}$ is the initial mass flow rate of injected droplets, $m_{d,0}$ is the initial mass of the droplet, and Δm_d represents the change in the mass of the droplet as it moves through an element, i.e., the difference in the mass of the droplet between the inlet and outlet of an element.

Similarly, the exchange of momentum appears in the continuous momentum equation in the form of the source term S_M , which is calculated as

$$S_M = S_x \mathbf{e}_x + S_r \mathbf{e}_r = \left[F_D(\mathbf{v} - \mathbf{v}_d) + \mathbf{g} \frac{(\rho_d - \rho)}{\rho_d} \right] \dot{m}_d \Delta t \quad (26)$$

where \dot{m}_d is the droplet mass flow rate, and Δt is the time step.

Finally, the volumetric heat source S_h appearing in the energy equation represents the heat transfer from the continuous phase to the discrete phase as a droplet passes through a cell, and is computed as

$$S_h = \left[\frac{\bar{m}_d}{m_{d,0}} c_{p,d} \Delta T_d + \frac{\Delta m_d}{m_{d,0}} \left(-h_{fg} + \int_{T_{ref}}^{T_d} c_{p,d} dT \right) \right] \dot{m}_{d,0} \quad (27)$$

where \bar{m}_d is the average mass of the particle in a cell.

Model description

Numerical method

The problem is solved using the FLUENT commercial CFD package, which adopts a cell centered finite volume method [32, 33] for the discretization of the continuous phase equations. Therefore, the computational domain is decomposed into many nonoverlapping cells and solutions are obtained at their centroids. The conservation equations (1)–(7) are integrated over each element in the domain and transformed into algebraic equations. The collection of these algebraic equations over the entire computational domain results in systems that are solved for the unknown variables. The coefficients of these algebraic equations are composed of contributions resulting from the discretization of the various terms in the original conservation equations. Convection and diffusion fluxes are evaluated at the faces of the cells, while sources are computed at element centroids. The diffusion term is decomposed in the contravariant directions [34, 35] with the part in the direction of the line connecting the centroids of the elements straddling the face discretized implicitly using a second-order central difference scheme, while the nonorthogonal part treated explicitly following a deferred correction approach. The convective fluxes are approximated using a second-order upwind scheme also implemented using the deferred correction practice [36]. Mass flow rates at elements faces are calculated using the Rhie–Chow interpolation technique [37] to eliminate the possibility of formation of checkerboard fields. The pressure–velocity coupling is resolved using the SIMPLE algorithm [38].

Before computing the discrete phase trajectory and obtaining the discrete phase source terms, the flow field is first initialized. The set of coupled ordinary differential equations of the discrete phase are solved by stepwise integration over discrete time steps using a semi-implicit trapezoidal scheme. The continuous phase is then calculated with the inclusion of the source terms adopted from the discrete phase. The discrete phase is then recalculated using the new flow field of the continuous phase. The process is repeated until a converged solution is achieved.

User-defined function

A UDF to calculate moist air density, overwrite the buoyancy forces calculated by the code, and extract additional psychrometric variables not computed in the package is written and hooked to FLUENT.

Mixture density

For psychrometric calculations, quantities are computed based on a unit mass of dry air (not unit mass of the mixture). The humidity ratio (W) represents the mass of water vapor per unit mass of

dry air and is computed in each cell as

$$W = \frac{Y_v}{1 - Y_v} \quad (28)$$

The density of dry air $\rho_{\text{dry air}}$ is calculated using the well-known ideal gas equation of state. Making use of W and $\rho_{\text{dry air}}$, the density of moist air is extracted using

$$\rho_{\text{moist air}} = \rho_{\text{dry air}} \frac{1 + W}{1 + 0.609 \times W} \quad (29)$$

Buoyancy force

The reference density ρ_{ref} is calculated at the reference temperature T_{ref} using the ideal gas equation of state. Then the buoyancy force due to density difference is computed and added as a source term in the momentum equation according to

$$F_{\text{buoyancy}} = \mathbf{g}(\rho_{\text{mixture}} - \rho_{\text{ref}}) \quad (30)$$

Relative humidity

An additional functionality of the UDF is the calculation of the relative humidity ϕ of the gas phase (i.e., moist air). Assuming moist air to behave as an ideal gas, ϕ is computed as [39]

$$\phi = 100 \times \frac{p_w}{p_{ws}} \quad (31)$$

where p_w is the partial pressure of water vapor given by

$$p_w = \frac{p \times W}{W + 0.62198} \quad (32)$$

and p_{ws} is the partial pressure of water vapor at saturation, which depends on the dry bulb temperature T of the gas phase, and is computed for the range of temperature involved using the following relation [39]:

$$p_{ws} = \exp\left(\frac{C_8}{T} + C_9 + C_{10} \times T + C_{11} \times T^2 + C_{12} \times T^3 + C_{13} \ln(T)\right) \quad (33)$$

where the coefficients can be found in [39].

Boundary conditions

The tower considered in this study is a vertical hollow cylinder of height H and diameter D (Figure 1). Air enters at the top of the tower where water is sprayed. Wind catchers are used to direct the wind into the tower, which are not modeled in the current study. The flow is assumed to be axisymmetric. A total pressure is imposed at inlet with the velocity direction assumed normal to the inlet plane. Mathematically the total pressure $p_{o,H}$ at inlet is given by

$$p_{o,H} = p_{s,H} + \frac{1}{2} \rho v_{\text{wind},H}^2 \quad (34)$$

where $p_{s,H}$ is the static pressure at height H calculated following the US standard atmosphere model, and $v_{\text{wind},H}$ is the prevailing wind speed at height H above the earth's surface. Therefore, depending on the conditions at inlet to the tower, air may be accelerated or decelerated with static pressure transformed into dynamic pressure and vice versa, leading to an increase or decrease in the air mass flow rate entering the tower. This is in essence the purpose of spraying water, which is expected to enhance the downdraft by increasing the entrained air mass flow rate at inlet. The air temperature and water

vapor in atmospheric air are also assigned values. For the droplet phase, the injected liquid water mass flow rate and temperature are given. Water is uniformly sprayed over the inlet cross-sectional area following a surface injection technique. For all cases, water droplets enter the domain at a temperature of 290 K. The no slip boundary condition is applied on the tower wall, which is assumed to be insulated. At outlet from the domain, a zero-normal gradient is applied on all variables.

Model validation

The model is validated by comparing its predictions with measured data reported in Ref [22], from a PDEC test facility located in Catania, Sicily at the Conphoebus Institute. The facility, shown in Figure 2 [40], is composed of a Tower with dimensions $4.1 \text{ m} \times 4.4 \text{ m} \times 10.7 \text{ m}$, a wind catcher at the top, and two rooms connected at the north and south sides of the tower each $6 \text{ m} \times 3.6 \text{ m} \times 4 \text{ m}$.

The wind catcher is composed of a metallic structure with two adjustable louvers of dimensions $1.7 \text{ m} \times 3.7 \text{ m}$ in the east-west direction to capture wind according to the prevailing wind direction. After wind is captured at the top, a straightener directs the wind toward a micronizer spray system composed of four circuits; each circuit has the number of nozzles shown in Table 1a, while each nozzle has a water flow rate of 7 L/h. The total number of nozzles is 20, giving the facility flexibility to inject water from 7 L/h up to 140 L/h. Depending on external ambient conditions and indoor requirements [40], an optimal flow rate is calculated and discharged by the spray system. The droplets are assumed to be $30 \mu\text{m}$ in diameter.

Sensors placed at five different locations of the outlet section measure the temperature and relative humidity of the air exiting the tower. As shown in Table 1b, seven cases having different external ambient temperature (T_{amb}) and relative humidity (ϕ_{amb}) are considered [22]. Results generated by the model are compared in Figure 3 with measured data. Figure 3a compares predicted (T_p) and measured (T_m) average temperatures while Figure 3b reports a similar comparison between



Figure 2. Passive downdraft evaporative cooling experimental test facility [40].

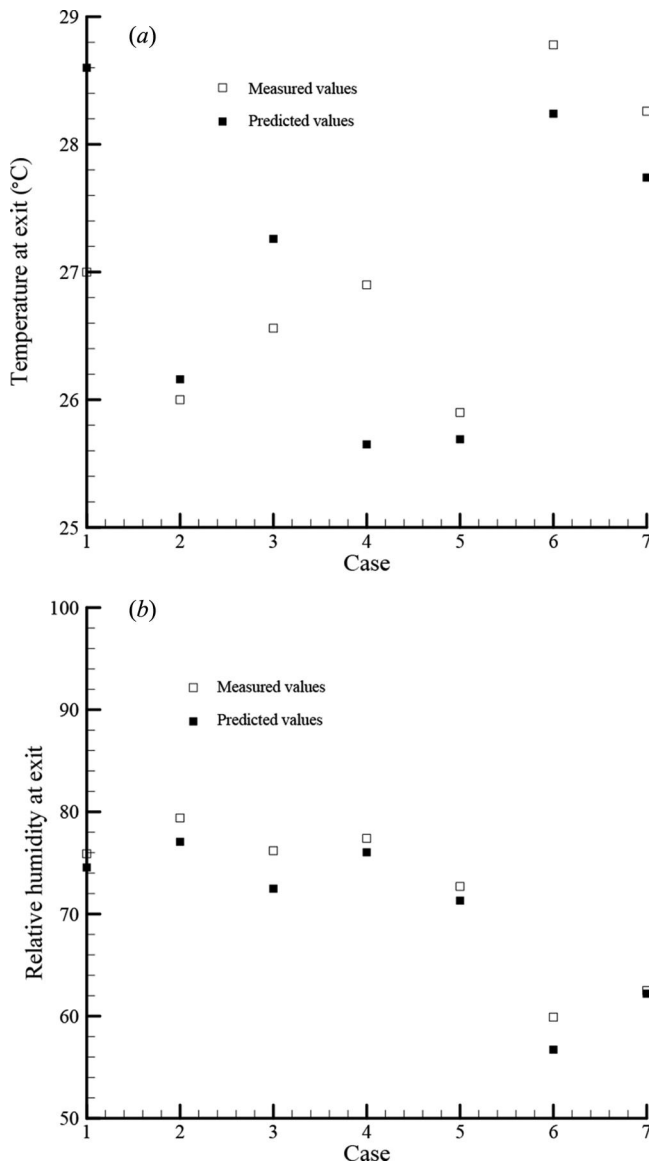
Table 1a. The micronizer spray system of a PDEC test facility [22].

Circuit #	# of Micronizers	Total flow rate (L/h)
1	2	14
2	4	28
3	6	42
4	8	56

PDEC, passive downdraft evaporative cooling.

Table 1b. Boundary conditions for the experimental facility [22].

Case	T_{amb} (°C)	Φ_{amb} (%)
1	31.7	62.9
2	31.0	55.7
3	32.5	50.7
4	33.0	45.4
5	36.9	29.0
6	37.4	27.7
7	37.9	28.0


Figure 3. Comparison between measured [22] and predicted (a) average temperature and (b) relative humidity at exit from the PDEC tower. Note: PDEC, passive downdraft evaporative cooling.

predicted (ϕ_p) and measured (ϕ_m) average relative humidity values at the exit of the PDEC tower. As shown, results are in good agreement with a maximum difference in temperature and relative humidity between predictions and measurements of 5.93 and 5.30%, respectively.

Results and discussion

The validated model is used to perform a parametric study on towers of different heights. The considered towers are hollow cylinders with their height to diameter ratio, unless otherwise stated, fixed at 2.5. Four towers of heights 20, 100, 400, and 1,000 m are investigated. For each tower the effects of varying the injection rate, droplet diameter, ambient air temperature, and outdoor relative humidity on performance is investigated. This is in addition to studying the influences of changing the tower height at fixed diameter and the tower diameter at fixed height on functioning. Exit conditions are evaluated at the outlet section before diverting the airflow into channels where the turbines are located.

The grid independence of results is established by generating solutions in a 100 m tower using two meshes with sizes of 100,000 and 196,000 elements. Grid systems are generated by adopting a mapped face meshing technique with near wall refinement. The variations in air density, pressure, temperature, and axial velocity over the tower height are compared in [Figures 4a–4d](#), respectively. As shown, results are on top of each other justifying the use of 100,000 elements. Similar tests performed for other heights confirmed that grid independent solutions for towers with heights of 20, 400, and 1,000 m are obtained using grid systems with sizes of 32,000, 200,000, and 310,000 elements, respectively.

A base case (BC) is considered against which the performance of the energy tower under other conditions is compared. The BC represents a hot and dry region with an outdoor temperature and relative humidity with values of 309.15 K and 13%, respectively. The droplet diameter and its temperature are considered to have the values 50 μm and 290 K, respectively.

The base case is compared with two other conditions; the first is a cold and dry condition obtained from the BC by decreasing the outdoor temperature to 25°C (298.15 K), and the second is a hot and humid condition obtained from the BC by increasing the outdoor relative humidity to 50%. All other parameters are kept constant.

Impact of injection rate

Computations are performed to study the effects of varying the water mass flow rate on the performance of the solar wind energy tower for the hot and dry (BC), cold and dry, and hot and humid conditions. Predictions are reported in [Figures 5–8](#) for an energy tower with height of 20, 100, 400, and 1,000 m, respectively. Results show the variations, with varying the water injection rate, of the average air density ([Figures 5a–8a](#)), relative humidity ([Figures 5b–8b](#)), temperature ([Figures 5c–8c](#)), and velocity ([Figures 5d–8d](#)) at exit from the tower. Profiles presented in the figures indicate that the trend of results is independent of the tower height.

As the water injection rate increases, the average moist air density ([Figures 5a–8a](#)), relative humidity ([Figures 5b–8b](#)), and velocity ([Figures 5d–8d](#)) increase, while its temperature decreases ([Figures 5c–8c](#)). Sensible heat is absorbed from the air by saturated liquid water to change phase to saturated vapor, which decreases the air temperature ([Figures 5c–8c](#)). A decrease in moist air temperature and/or an increase in water vapor in moist air cause an increase in the air relative humidity, indicating that the capacity of moist air to hold more water vapor is decreasing. The rate of increase in relative humidity shown in [Figures 5b–8b](#) is seen to be higher than the rate of increase/decrease in other variables and this is due to the double effect caused by the decrease in temperature and the increase in the humidity ratio (i.e., the amount of water vapor in air). Once saturation is reached (i.e., ϕ becomes 100%) no additional liquid water can be evaporated, the temperature reaches its saturation value (i.e., the wet bulb temperature of atmospheric air) and remains constant unaffected by

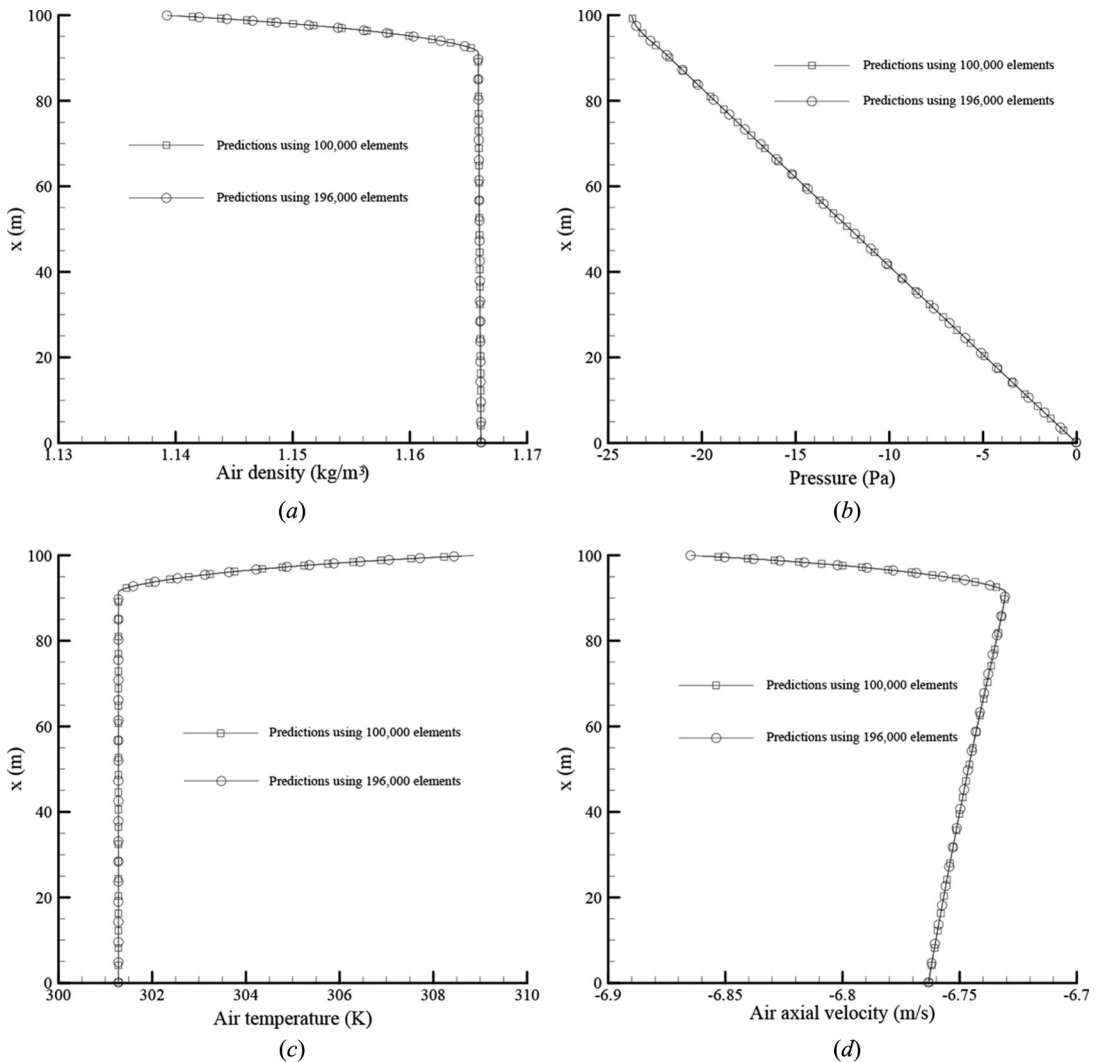


Figure 4. Comparison of air (a) density, (b) pressure, (c) temperature, and (d) axial velocity along the centerline of a solar wind energy tower of height 100 m and diameter 40 m generated using two grid systems with sizes of 100,000 and 196,000 elements.

increasing the water injection rate. Since within the range of temperature and pressure used moist air can be treated as an ideal gas, a decrease in air temperature is associated with an increase in its density (Figures 5a–8a), knowing that the pressure at exit is constant (atmospheric) independent of the injection rate. The increase in the average velocity of the air at exit from the energy tower clearly demonstrates the increase in the downdraft effect with an increase in the water injection rate (from continuity the average velocity of the air at inlet is only slightly different than the velocity at exit, see Figure 4d). Comparing Figures 5d–8d, velocity is the parameter affected by the channel height. The taller the tower, the higher is the air velocity. In all cases, as water injection rate increases the rate of change in exit conditions decreases because air cannot hold water beyond saturation.

By comparing profiles within a plot in Figures 5–8, it is obvious that a larger amount of water evaporates when the air is hotter, as warmer air can hold more water vapor. Therefore, the ideal situation for evaporation is a hot and dry condition (i.e., the BC). Results show that the tower performs best under the BC conditions followed by the cold and dry conditions ($T_{\text{inlet}} = 25^\circ\text{C}$), and finally the hot and humid conditions ($\phi_{\text{inlet}} = 50\%$). The highest average velocity is achieved with the hot and

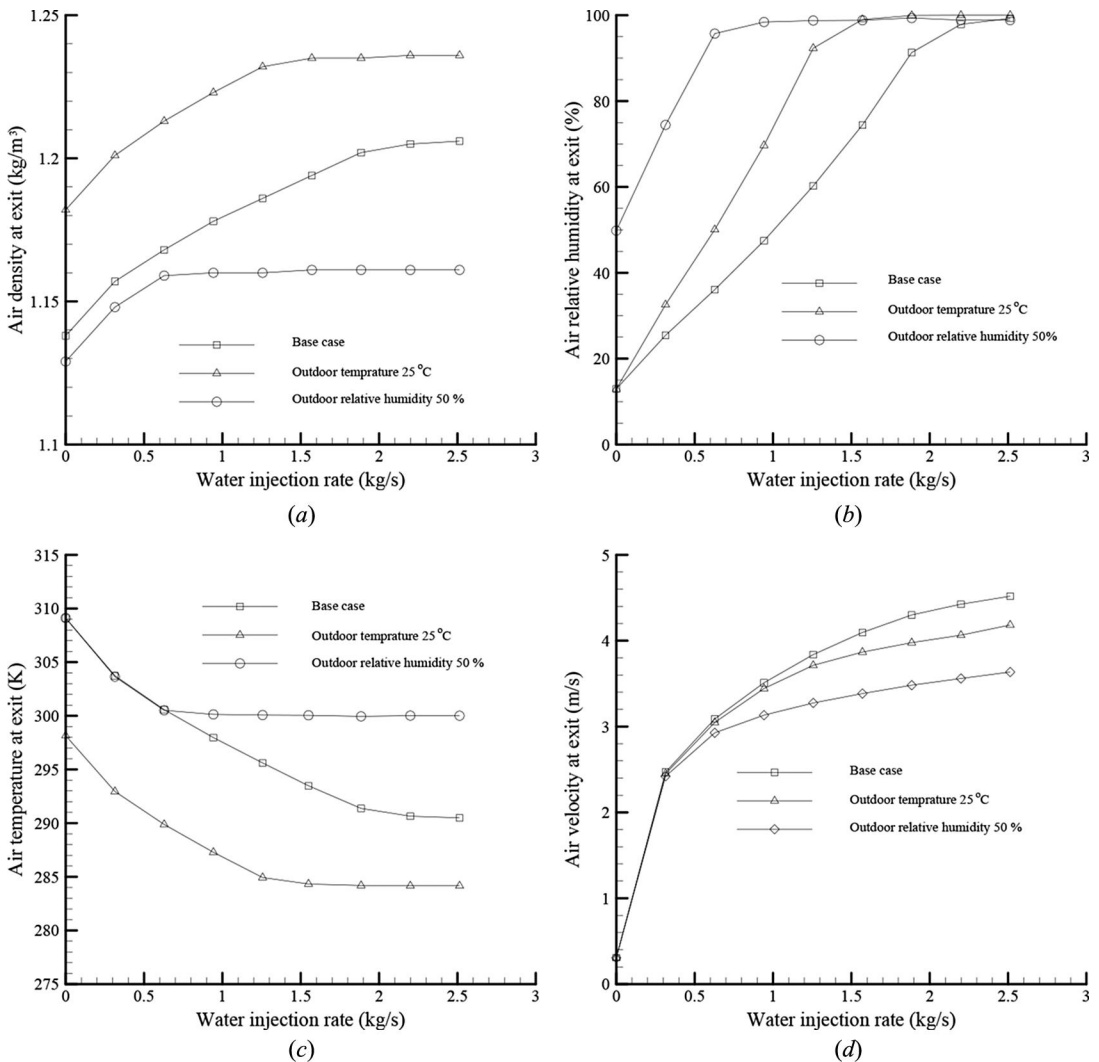


Figure 5. Effect of water injection rate on average air (a) density, (b) relative humidity, (c) temperature, and (d) velocity at exit from a solar wind energy tower of height 20 m and diameter 8 m.

dry weather conditions, reaching 4.51, 10.57, 21.01, and 33.17 m/s for an energy tower with height of 20, 100, 400, and 1,000 m, respectively. Moreover, predictions demonstrate that saturation is achieved faster in a humid environment. This is to be expected as moist air enters the domain holding a larger amount of water than for other weather conditions. This is followed by the cold and dry conditions, with the hot and dry conditions (i.e., the BC) being capable of evaporating the largest quantity of water.

Impact of ambient conditions

In this section, the effects of varying the ambient temperature at constant relative humidity and varying the ambient relative humidity at constant temperature is investigated in an energy tower of height 20 m and diameter 8 m ($H/D = 2.5$) for different injection rates. In the first set of results (Figure 9a) the outdoor relative humidity is fixed at 13% and the outdoor temperature is assigned consecutively the values of 20, 25, 30, and 36°C. In the second set of results (Figure 9b) the outdoor

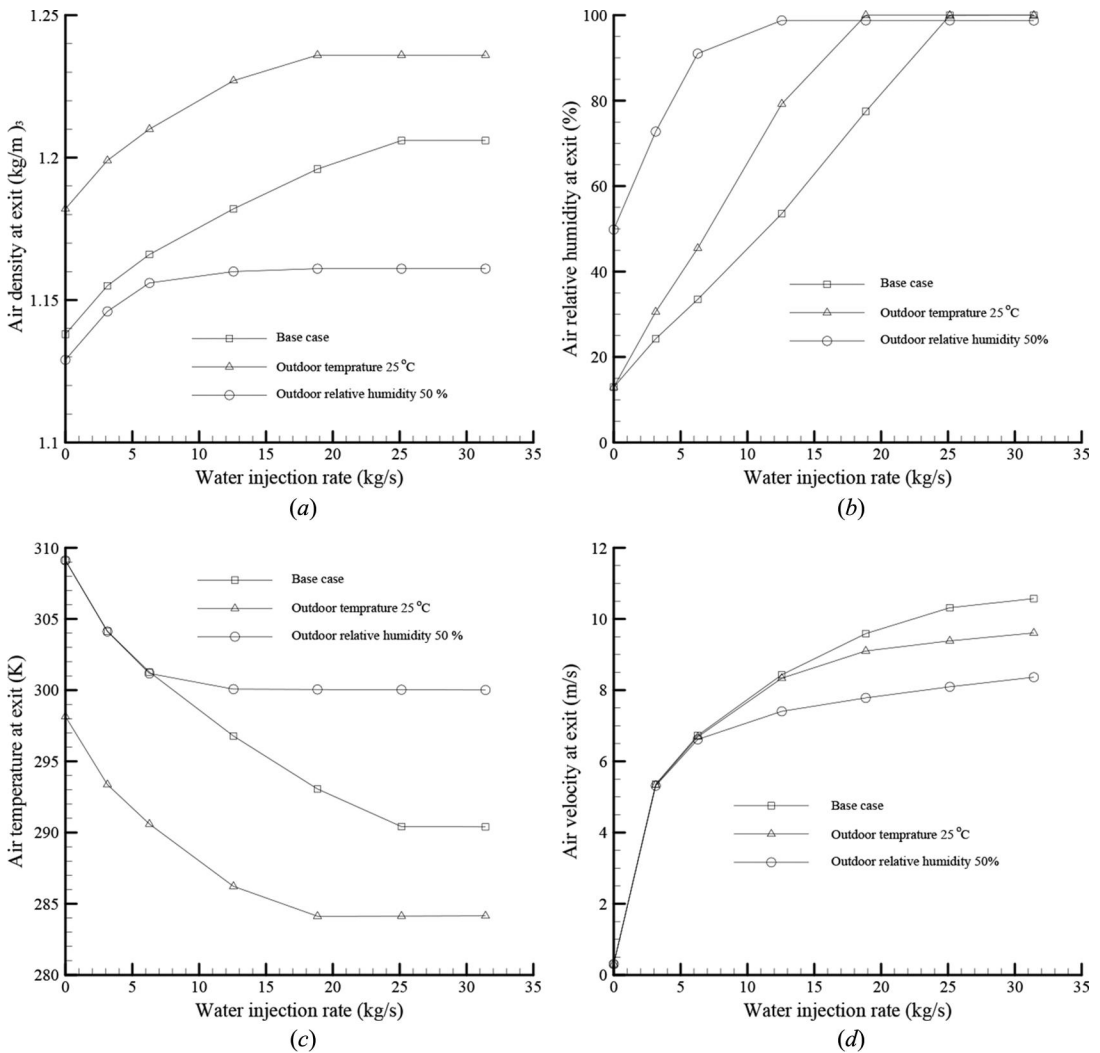


Figure 6. Effect of water injection rate on average air (a) density, (b) relative humidity, (c) temperature, and (d) velocity at exit from a solar wind energy tower of height 100 m and diameter 40 m.

temperature is fixed at 36°C and the outdoor relative humidity is assigned consecutively the values of 13, 25, 50, and 75%. Figures 9a, b show the exit velocity as a function of outdoor temperature and outdoor relative humidity, respectively, for different values of the water injection rate.

The strength of the downdraft is mainly driven by the difference in temperature between the outdoor air and the air flowing inside the tower. The amount of water that can be evaporated into air is limited by the difference between the dry bulb and wet bulb temperature (the process may be approximated as an evaporative cooling process occurring along a line of constant wet bulb temperature).

At the lowest injection rate of 0.31 kg/s, all droplets evaporate in the upper part of the tower and the temperature drop over the range of ambient temperature varies between 5.1 and 5.3 for temperatures of 20 and 36°C, respectively. This is translated into a negligible downdraft intensity difference ranging from 2.43 to 2.47 m/s (Figure 9a). By increasing the water injection rate for saturation to be achieved, the air temperature at saturation drops to its wet bulb temperature value. For an outdoor relative humidity of 13%, the wet bulb temperatures at dry bulb temperatures of 20, 25, 30, and 36°C

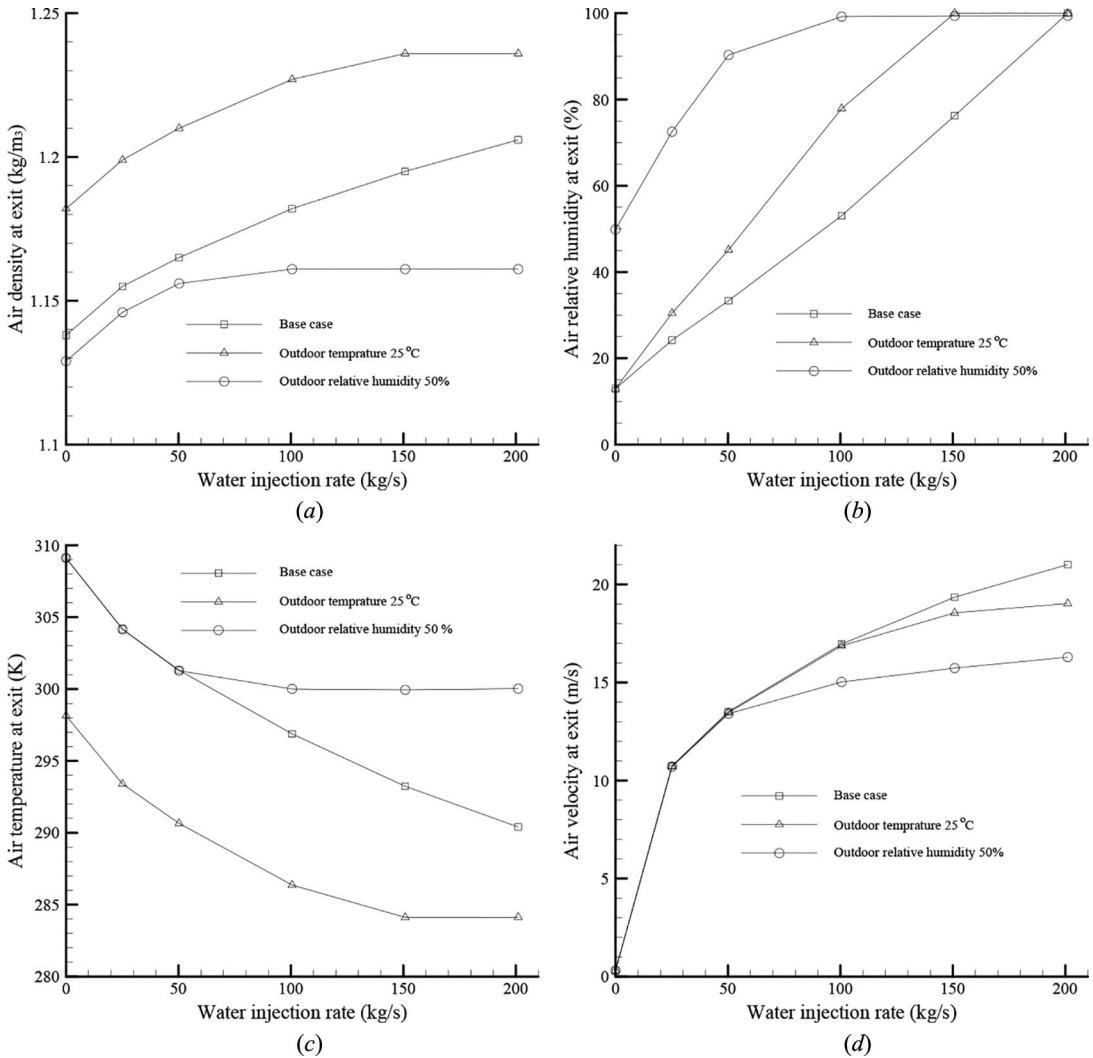


Figure 7. Effect of water injection rate on average air (a) density, (b) relative humidity, (c) temperature, and (d) velocity at exit from a solar wind energy tower of height 400 m and diameter 160 m.

are 8.11, 11.1, 14, and 17.39°C, respectively. Consequently, the maximum possible drops in air temperatures are 11.89, 13.9, 16, and 18.61°C, respectively. Therefore, at a given relative humidity, a higher ambient temperature leads to a higher cooling potential and eventually a stronger downdraft (Figure 9a). It is only at high injection rate that the difference in performance of the tower becomes evident. For instance, when the ambient temperature is 20°C, an injection rate of 0.94 kg/s brings the exit temperature very close to the wet bulb temperature. Therefore, any increase in the injection rate will not appreciably enhance the performance of the tower. Whereas when the ambient temperature is 36°C, an injection rate of 0.94 kg/s yields a temperature drop of only 11.14°C while it is possible to decrease the temperature by 18.61°C. This is why a more intense downdraft is obtained for an ambient air temperature of 36°C in comparison with a temperature of 20°C (Figure 9a). Results reported in Figure 9a indicate that the air average velocity at exit from the energy tower (and consequently the power that can be extracted) increases with increasing air ambient temperature and/or increasing water injection rate.

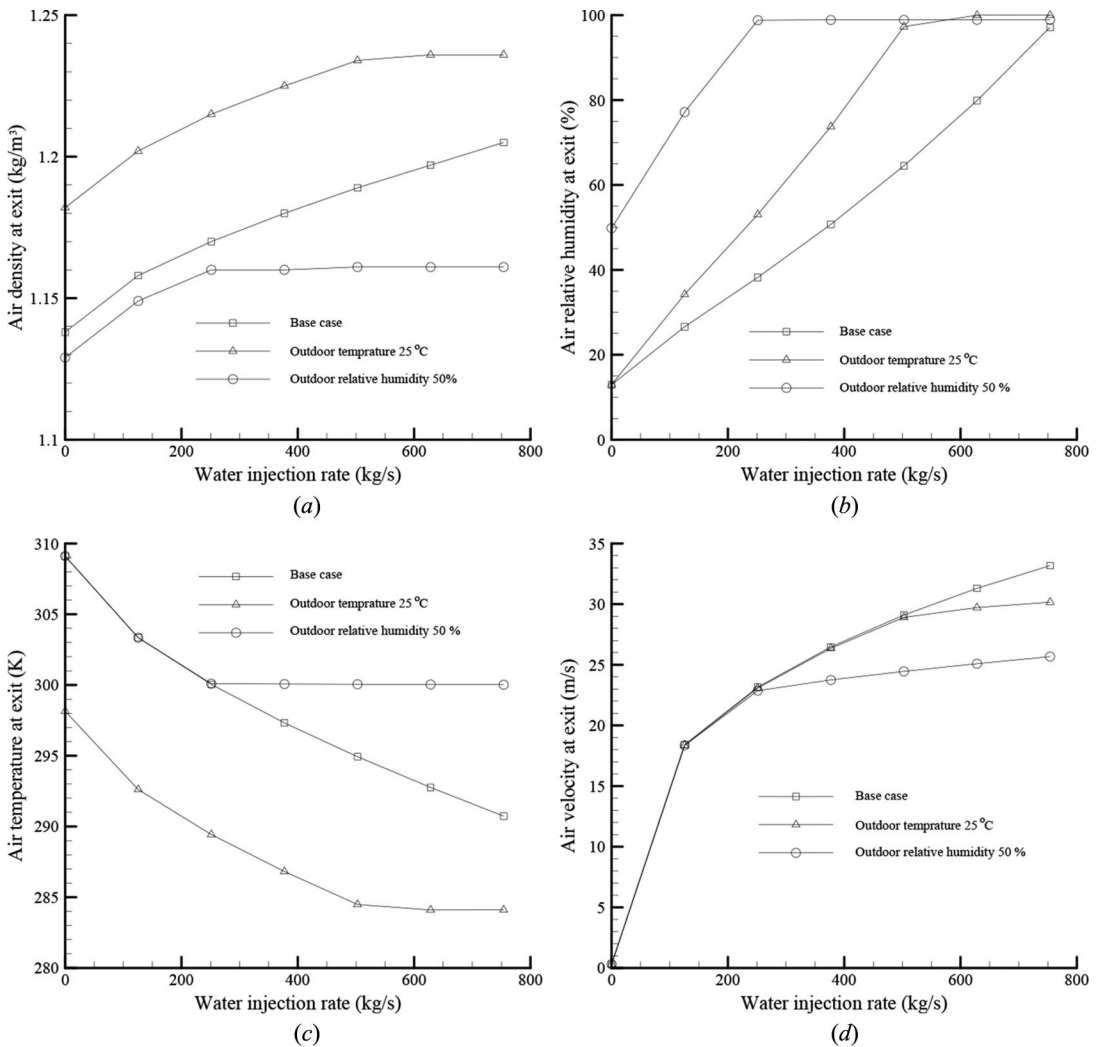
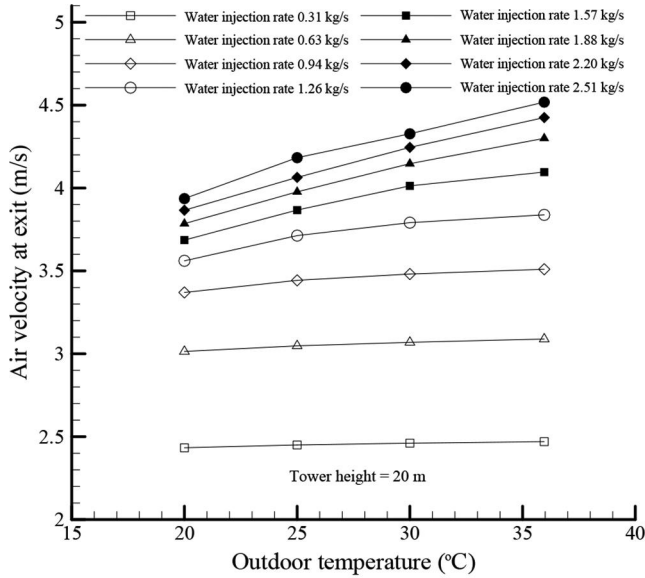


Figure 8. Effect of water injection rate on average air (a) density, (b) relative humidity, (c) temperature, and (d) velocity at exit from a solar wind energy tower of height 1,000 m and diameter 400 m.

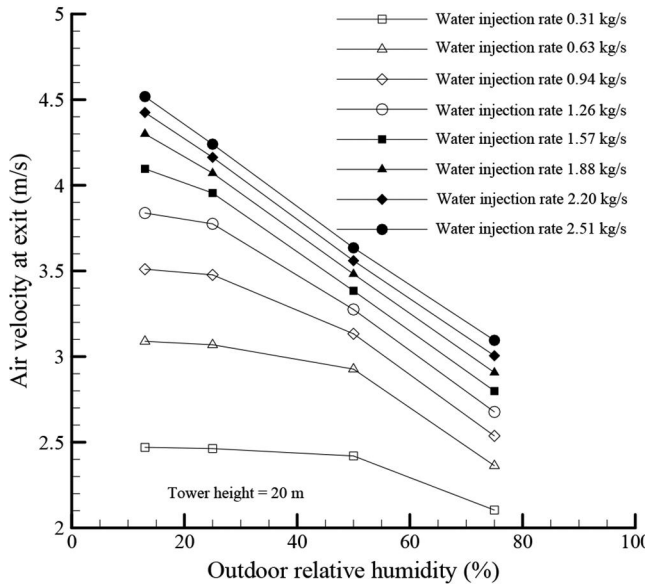
Similarly, [Figure 9b](#) demonstrates that the highest exit velocities are achieved at the lowest outdoor relative humidity (i.e., 13%). The average velocity of the air at exit decreases with increasing the ambient relative humidity and increases with increasing the water injection rate. For an ambient temperature of 36°C, the maximum drops in air temperature for relative humidity values of 13, 25, 50, and 75% are 18.75, 15.08, 9.02, and 4.12°C, respectively. For an outdoor relative humidity of 75%, injecting 0.31 kg/s will quickly bring the exit temperature close to the wet bulb temperature, and therefore injection rates exceeding 0.31 kg/s have small impact on temperature drop, which translates into a relatively small change in exit velocity in comparison with the change at low relative humidity.

Droplet evaporation

The droplet evaporation process is illustrated in [Figure 10](#) by presenting at different injection rates the variation in the diameter of a droplet as it moves inside a 100 m high energy tower. The analysis is



(a)



(b)

Figure 9. Effect of outdoor (a) temperature and (b) relative humidity on average air velocity at exit from a solar wind energy tower of height 20 m and diameter 8 m.

done considering the base case conditions with injected water droplets of size 50 μm . As shown, the evaporation process is gradual. For low injection rates, the droplet evaporates within the first 18 m of the tower. For the highest injection rates considered (25.13 and 31.42 kg/s) the domain becomes saturated within the top 80 and 50 m, whereby the droplet diameter is reduced from 50 to 5 and 30 μm , respectively. Therefore, as a droplet continues descending (beyond 80 and 50 m, respectively), it no longer changes size as air becomes saturated incapable of holding more vapor and consequently suppressing the evaporation process.

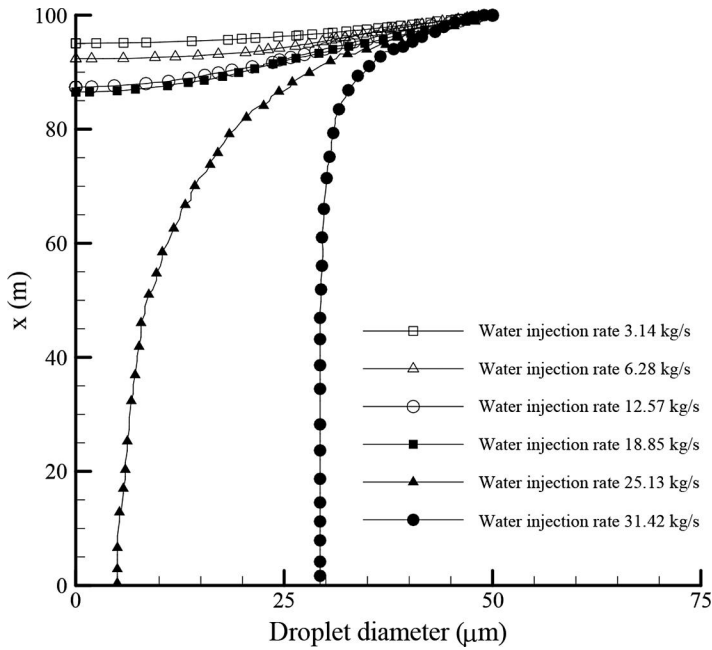


Figure 10. The decrease in the size of a 50 μm water droplet due to evaporation as it moves downward in a tower of height 100 m and diameter 40 m for different water injection rate values.

Flow field evolution

The effects of varying the water injection rate and droplet diameter on the axial variations of the flow field properties along the centerline of a 20 m energy tower are studied. The base case conditions are considered and predictions are presented in Figure 11. The figure displays the axial profiles of the air density (Figures 11a, b), relative humidity (Figures 11c, d), and temperature (Figures 11e, f). The effects of varying the water injection rates can be inferred from Figures 11a, c, e, while the influences of changing the droplet diameter can be deduced from Figures 11b, d, f. When varying the water injection rate, the droplet diameter is held fixed at 50 μm ; when changing the droplet diameter, a water injection rate with value of 0.63 kg/s is used. In all cases, evaporation increases the air density and relative humidity and decreases temperature for the reasons discussed earlier.

At low injection rates, all water droplets evaporate in the upper part of the tower. Consequently, variations in properties occur in that section and become constant afterwards. When the injection rate increases, variations in properties extend over the channel height and the rate of variation decreases as saturation is approached and evaporation becomes more gradual. Moreover, once the injected quantity is capable of causing saturation, injecting additional water has a minor effect on exit conditions.

With an increase in the droplet size for the same quantity of injected water (i.e., 0.63 kg/s), the contact surface area between droplets and air decreases. For example as the droplet diameter is doubled, the surface area is halved. Therefore, a longer distance (taller tower) is required to evaporate the same quantity of water, as revealed by the axial profiles shown in Figures 11b, d, f. Carlson [1] suggested that the droplet diameter should not exceed 100 μm for all droplets to evaporate. In Figures 11b, d, f, the exit conditions for the droplets with size of 100 μm become constant toward the exit of the tower, indicating complete evaporation within the domain. For droplet sizes greater than 100 μm , droplets leave the domain not fully evaporated since the evaporation is reduced due to an increase in the droplet size, which is associated with a decrease in the evaporation area. Moreover, the rate of evaporation decreases as the droplet size increases. The slightly lower

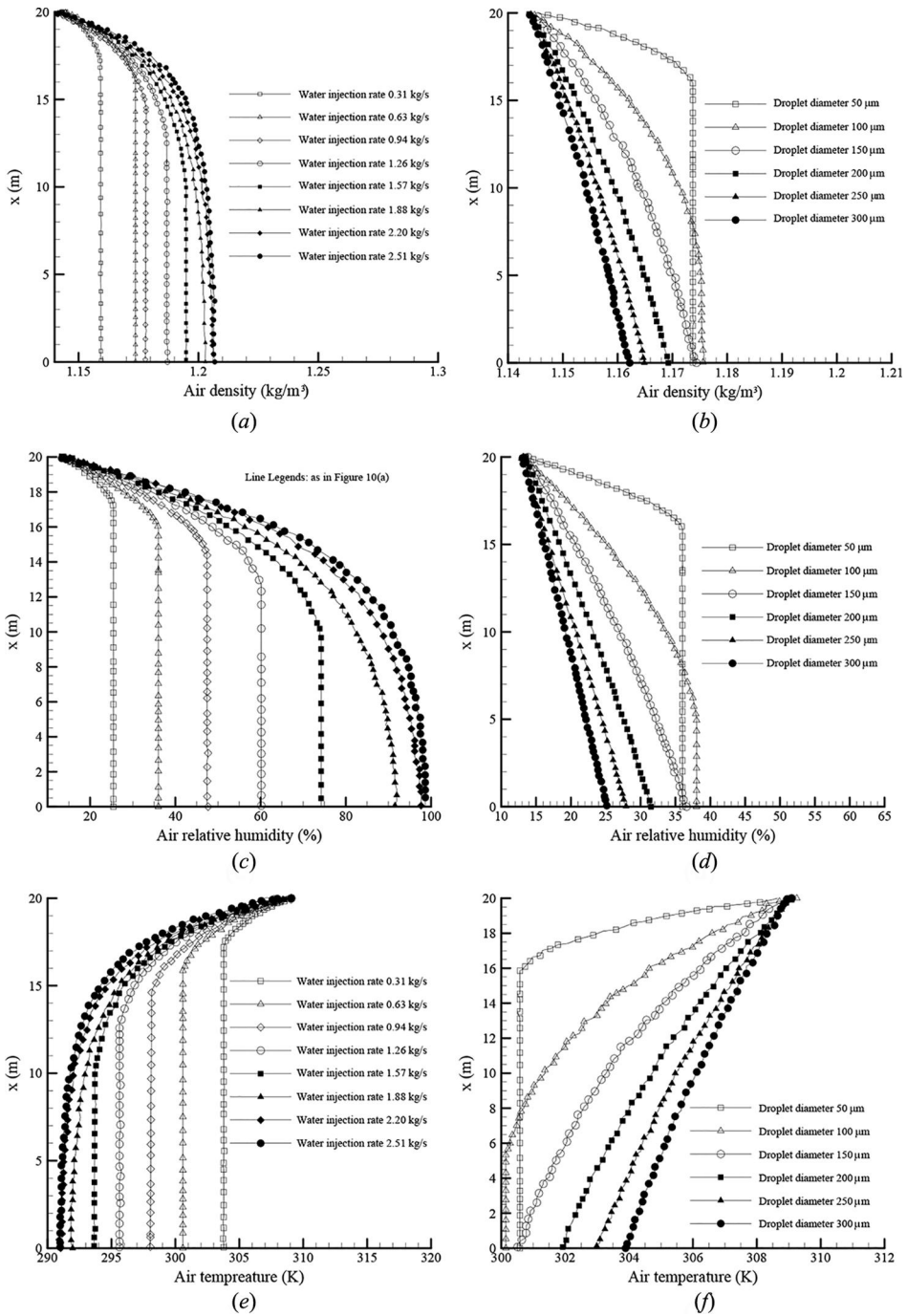


Figure 11. Variation of air (a, b) density, (c, d) relative humidity, and (e, f) temperature along the centerline of a solar wind energy tower of height 20 m and diameter 8 m for different (a, c, e) water injection rates and (b, d, f) droplet diameters.

temperature and higher density and relative humidity predicted with droplets of size 100 μm in comparison with droplets of size 50 μm, even though the same quantity of water was evaporated in both cases, is only a local effect as variations are presented along the tower centerline and do not represent average values.

Enhancement of the entrained air mass flow rate by water injection

The enhancement in the mass flow rate that can be produced by an energy tower due to water injection is represented by Q , which is equal to the ratio of mass flow rate produced with water injection to the mass flow rate in the tower without water injection.

Figure 12a illustrates, for a 20 m energy tower, the variation of Q with varying the ambient conditions for different water injection rates. Using the base case as a reference, outdoor air temperature

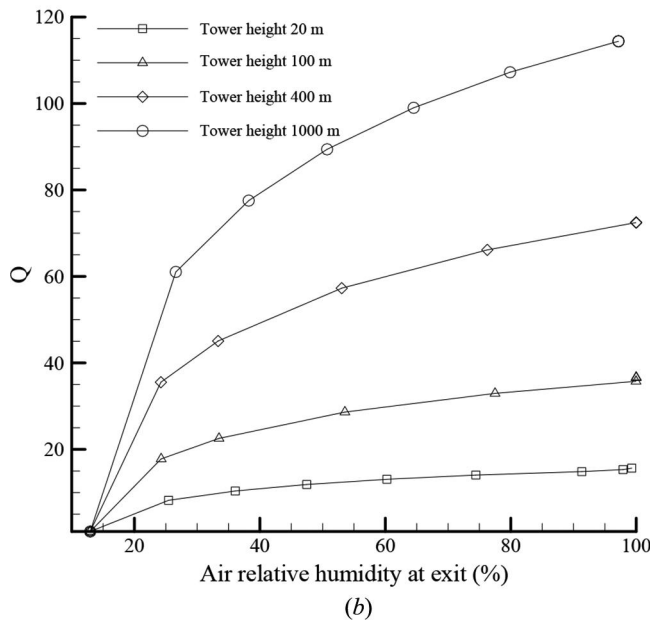
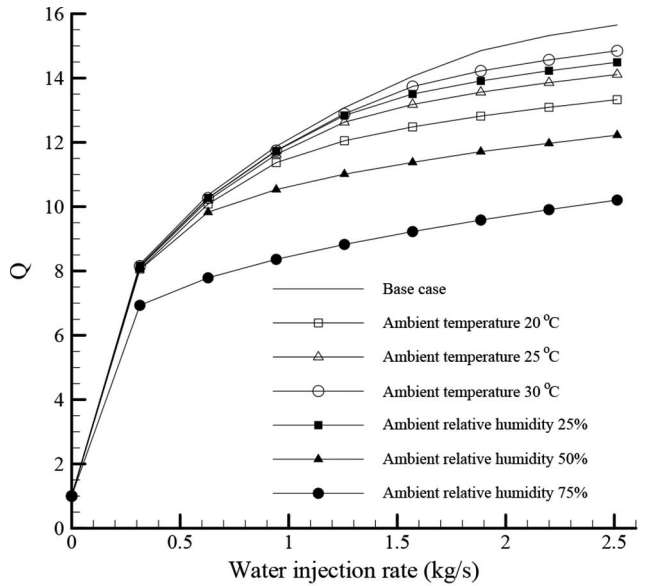


Figure 12. Variation of Q (the ratio of mass flow rate produced with water injection to the mass flow rate in the tower without water injection) (a) with water injection rate for different outdoor conditions for a tower of height 20 m and diameter 8 m, and (b) with air relative humidity at exit for towers of different heights.

values of 20, 25, and 30°C and relative humidity values of 25, 50, and 75% are considered. It is observed that the tower performs best in the base case; injecting 2.5 kg/s of water produces 15.6 times the air mass flow rate that could be produced without water injection. The poorest performance of the tower is obtained with an outdoor relative humidity of 75%.

The variation of Q is also studied for all tower heights using the base case conditions. Predicted values, which are presented in Figure 12b, are plotted as function of the air relative humidity at exit from the tower. For every tower height, the rate of water injection varies between zero and a maximum value sufficient to produce saturated air at exit. Since towers are of different heights, different water injection rates are used. At low injection rates, the rate of change of Q is high as air is still relatively dry and capable of absorbing water vapor. As saturation is approached, the rate of increase in Q diminishes as the evaporation rate decreases. Furthermore, predictions indicate that the mass flow rate of entrained air increases as the tower height increases and reaches the value of 115, 72, 35, and 15.6 for a tower with height of 1,000, 400, 100, and 20 m, respectively. The relationship between Q_{max} and tower height (for a fixed height to diameter ratio with value of 2.5) is correlated through the following equation:

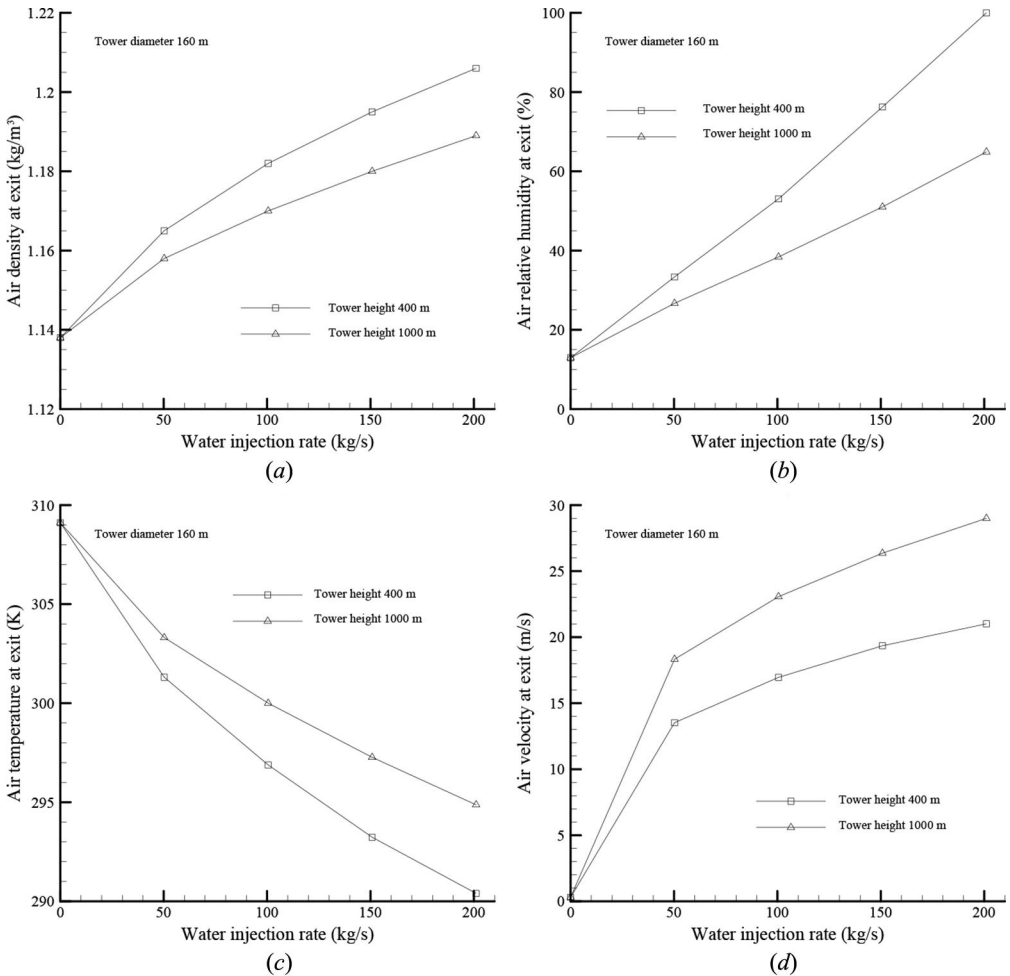


Figure 13. Effect of the height of a solar wind energy tower on average air (a) density, (b) relative humidity, (c) temperature, and (d) velocity at exit for different water injection rates.

$$Q_{\max} = 3.62\sqrt{H} \quad (35)$$

with a maximum error less than 0.5%.

Impact of tower height

The effect of tower height on performance is reported here by comparing the air average density (Figure 13a), relative humidity (Figure 13b), temperature (Figure 13c), and velocity (Figure 13d) obtained for two towers of heights 400 and 1,000 m. Using the base case conditions, values are predicted for different water injection rates while holding the diameter constant at 160 m. The effect of height is included by calculating the total pressure at inlet based on the available wind speed (following the wind profile power law). The presence of wind catchers at inlet, which are not physically modeled, is accounted for by imposing a downward wind direction. Optimization of wind catchers at tower inlet that allow redirecting the air with minimum losses is not a target of this study.

Results displayed in Figure 13a–13d show that, at a given mass flow rate, increasing the tower height results in lower average density (Figure 13a) and relative humidity (Figure 13b) and higher temperature (Figure 13c) and velocity (Figure 13d) at exit. Therefore, increasing the tower height enhances its performance by increasing the downdraft and allowing higher velocities to be obtained.

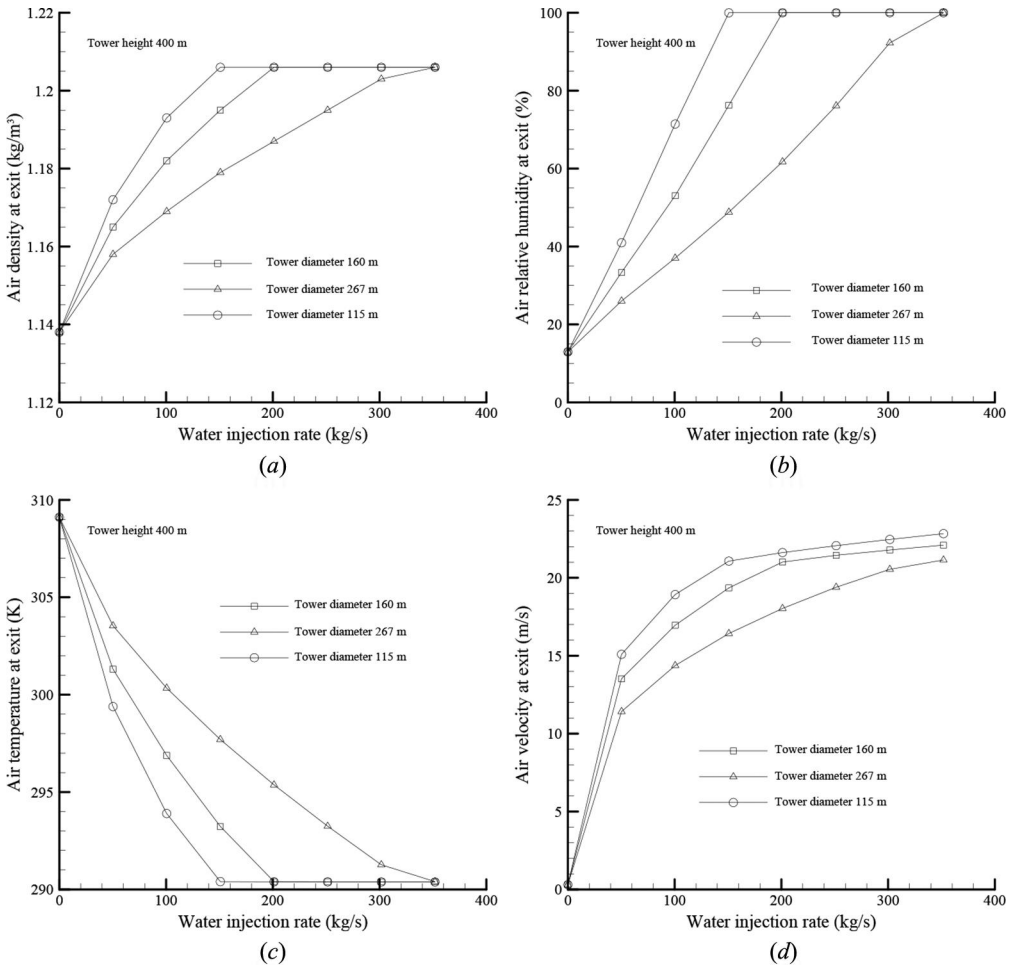


Figure 14. Effect of the diameter of a solar wind energy tower of height 400 m on average air (a) density, (b) relative humidity, (c) temperature, and (d) velocity at exit for different water injection rates.

For example, the velocity reaches 28.9 m/s in a 1,000 m tower versus 21 m/s for a 400 m tower at an injection rate of 200 kg/s. At this injection rate, saturation conditions are achieved in the 400 m tower, while it reaches only 65% in the 1,000 m tower. Thus, injecting more water will not enhance the performance of the 400 m tower since air is already saturated. However, the performance of the 1,000 m tall tower will be further improved as the flowing air is still capable of evaporating additional water.

Impact of tower diameter

The height of the energy tower is fixed at 400 m and its diameter is assigned the values of 115, 160, and 267 m corresponding to values of the height to diameter ratio of 3.5, 2.5, and 1.5, respectively. Simulations in the three towers are conducted subject to the base case conditions and predictions are compared in Figure 14. Figure 14a–d depict, respectively, the variations in the average air density, relative humidity, temperature, and velocity at exit from the towers as function of the water injection rate.

Saturation conditions (Figure 14b) are achieved first in the tower of diameter 115 m at an injection rate of 150 kg/s; second in the tower of diameter 160 m at an injection rate of 200 kg/s; and last in the tower of diameter 267 m at an injection rate of 352 kg/s. This is because as the total volume of the tower increases, more water is needed to saturate the air inside. The variations in average density and temperature at exit follow the general trend presented earlier and once saturation is reached their values become the same independent of the tower diameter (i.e., density approaches 1.206 kg/m^3 and temperature approaches 290 K). Under this condition, the velocity at exit from the towers of diameter 115, 160, and 267 m is 21.6, 21.4, and 21.1 m/s, respectively. Therefore, the tower diameter has little effect on the average velocity and consequently Q . Furthermore, since at saturation the density in all towers is the same, it can be deduced that the saturated air mass flow rate for a given tower height and water injection rate is mainly controlled by the cross-sectional area of the tower.

Energy analysis

The power that can be extracted from a wind stream by a wind turbine [41] is given by

$$\begin{aligned} P_{\text{generated}} &= \eta_{\text{wind turbine}} \frac{161}{272} \dot{m}_{\text{air}} V_{\text{air,exit}}^2 \\ &= \eta_{\text{wind turbine}} \frac{161}{272} \rho_{\text{air}} \left(\frac{\pi D^2}{4} \right) V_{\text{air,exit}}^3 \quad \eta_{\text{wind turbine}} \approx 0.40 \end{aligned} \quad (36)$$

In this study, the rotor diameter of the turbine D is considered to be equivalent to the diameter of the tower. The power generated is computed based on the mass flow rate that will enable all water droplets to evaporate within the domain producing saturated conditions at tower exit. Not all power generated is available as a portion of it is required to pump water and run auxiliary equipment such as the injectors. In the analysis, the power consumed is computed based on the power required to pump water, which represents the largest portion. The power required to run auxiliary equipment is assumed to be accounted for in the pump efficiency, which is assigned a value of 70%. Thus, the consumed power is computed as

$$P_{\text{consumed}} = \frac{\dot{m}_{\text{water}} g H}{\eta_{\text{pump}}} \quad \eta_{\text{pump}} \approx 0.7 \quad (37)$$

The net power is computed based on the difference between the power generated and the power consumed and is calculated as

$$P_{\text{net}} = P_{\text{generated}} - P_{\text{consumed}} \quad (38)$$

The electric energy and power generated, displayed in Table 2a, are computed for all tower heights ($H/D = 2.5$) assuming an ambient temperature of 309.15 K, an outdoor relative humidity of 13%, and

Table 2a. Powers and energy output of an energy tower.

Tower height (m)	20	100	400	1,000
$P_{\text{generated}}$ (kW)	0.66	197.12	26,660.33	655,441.19
P_{consumed} (kW)	0.52	35.21	1,127.08	10,566.49
P_{net} (kW)	0.13	161.91	25,533.24	644,874.70
E_{net} (kWh/day)	1.62	1,942.93	306,398.95	7,738,496.44

Table 2b. Cost analysis of an energy tower.

Tower height (m)	20	100	400	1,000
Installation cost (M\$)	2.5	11	50	745
Annual O&M cost (c/kwh)	0.556	0.556	0.556	0.556
Total cost over 50 years (M\$)	2.5	11.2	81.1	1,530.2
Cost of electricity (\$/kwh)	84.161	0.315	0.014	0.011

droplets of size and temperature 50 μm and 290 K, respectively. The cost of electricity is displayed in Table 2b for the cases presented in Table 2a. The tower is assumed to operate 12 h a day when sunshine is available over a period of 50 years. The construction, operation, and maintenance costs are extracted from a study conducted by Zaslavsky et al. [42]. The calculations are performed based on present worth without accounting for future inflation and rate of return. The analysis shows that for towers of 20 and 100 m high the cost of electricity is expensive and commercially unfeasible. Whereas adopting tower heights of 400 and 1,000 m yields cheap electricity costing 0.014 and 0.011 \$/kwh, respectively.

Closing remarks

The performance of solar wind energy towers was investigated numerically. An Euler–Lagrange approach was adopted to resolve the two-phase flow of air and water droplets in the tower. The effects of tower height, tower diameter, water injection rate, ambient temperature, and ambient relative humidity on the strength of the downdraft current was assessed. It was found that hot and dry conditions are best for the operation of energy towers. The higher the ambient temperature the more water can be evaporated and the stronger will be the downdraft. Further, the lower is the ambient relative humidity, the higher will be the capability of the air to absorb water vapor and the stronger will be the downdraft. For a certain tower diameter, the higher the tower the stronger will be the downdraft at a given mass flow rate. At a given channel height, changing the tower diameter has no effect on the downdraft strength. The conducted energy analysis revealed that short towers are not economical while tall towers are highly competitive.

Funding

The financial support provided by the Munib R. and Angela Masri Institute of Energy and Natural Resources at the American University of Beirut through award number 103027 is gratefully acknowledged.

References

- [1] P. Carlson, “Power generation through controlled convection (aeroelectric power generation),” U.S. Patent 3,894,393 A, 1974.
- [2] D. Zaslavsky *et al.*, “Sharav Sluices Ltd files patent application for renewable resource hydro/aero-power generation plant and method of generating hydro/aero-power,” U.S. Patent 6,510,687 B1, 2011.
- [3] G. Abhinava, N. Swarnkar, S. Behera, and G. Edison, “Creation of artificial downdraft for wind power plant,” International Conference on Energy Efficient Technologies for Sustainability, Nagercoil, India, IEEE, pp. 571–576, 2013.
- [4] M. Bauer and I. Gasser, “Modeling, asymptotic analysis, and simulation of an energy tower,” *SIAM J. Appl. Math.*, vol. 72, no. 1, pp. 362–381, 2012.

- [5] A. A. Mostafa, "Modeling of densely loaded two-phase flows," *Numer. Heat Transfer, Part A*, vol. 20, no. 3, pp. 317–328, 1991.
- [6] M. Jicha, K. C. Karki, and S. V. Patankar, "Numerical analysis of water spray system in the entrance region of a two-dimensional channel using Lagrangian approach," *Numer. Heat Transfer, Part A*, vol. 26, no. 1, pp. 1–16, 1994.
- [7] X.-Q. Chen and J. C. F. Pereira, "Prediction of evaporating spray in anisotropically turbulent gas flow," *Numer. Heat Transfer, Part A*, vol. 27, no. 2, pp. 143–162, 1995.
- [8] M. Hallman, M. Scheurlen, and S. Wittig, "Computation of turbulent evaporating sprays: Eulerian versus Lagrangian approach," *J. Eng. Gas Turbines Power*, vol. 117, no. 1, pp. 112–119, 1995.
- [9] M. Burger *et al.*, "A combined Eulerian and Lagrangian method for prediction of evaporating sprays," *J. Eng. Gas Turbines Power*, vol. 124, no. 3, pp. 481–488, 2002.
- [10] S. Kondaraju and J. S. Lee, "Hybrid turbulence modeling of liquid spray impingement on a heated wall with arbitrary Lagrangian Eulerian method," *Numer. Heat Transfer, Part A*, vol. 42, no. 12, pp. 1059–1079, 2007.
- [11] K. Li and L. X. Zhou, "Studies of the effect of spray inlet conditions on the flow and flame structures of ethanol-spray combustion by Large-Eddy simulation," *Numer. Heat Transfer, Part A*, vol. 62, no. 1, pp. 44–59, 2012.
- [12] A. V. Nguyen, C. A. J. Fletcher, and J. Y. Tu, "Novel Eulerian formulation for dilute gas-particle flows with an obstruction," *Numer. Heat Transfer, Part A*, vol. 35, no. 7, pp. 735–756, 1999.
- [13] F. Nmira, A. Kaiss, J.-L. Consalvi, and B. Porterie, "Predicting fire suppression efficiency using polydisperse water sprays," *Numer. Heat Transfer, Part A*, vol. 53, no. 2, pp. 132–156, 2007.
- [14] M. A. Pakhomov and V. I. Terekhov, "Numerical modeling of turbulent flow structure and heat transfer in a droplet-Laden swirling flow in a pipe with a sudden expansion," *Numer. Heat Transfer, Part A*, vol. 71, no. 7, pp. 721–736, 2017.
- [15] F. Moukalled and M. Darwish, "Mixing and evaporation of liquid droplets injected into an air stream flowing at all speed," *Phys. Fluids*, vol. 20, no. 4, art. no. 040804, pp. 1–26, 2008.
- [16] F. Moukalled and M. Darwish, "Numerical prediction of dispersion and evaporation of liquid sprays in gases flowing at all speed," *Numer. Heat Transfer, Part B*, vol. 54, no. 3, pp. 185–212, 2008.
- [17] J. B. Greenberg, I. Silverman, and Y. Tambour, "On the origin of spray sectional conservation equations," *Combust. Flame*, vol. 93, nos. 1–2, pp. 90–96, 1993.
- [18] F. Laurent, M. Massot, and P. Villedieu, "Eulerian multi-fluid modeling for the numerical simulation of coalescence in polydisperse dense liquid sprays," *J. Comput. Phys.*, vol. 194, no. 2, pp. 505–543, 2004.
- [19] R. O. Fox, F. Laurent, and M. Massot, "Numerical Simulation of spray coalescence in an Eulerian framework: Direct quadrature method of moments and multi-fluid method," *J. Comput. Phys.*, vol. 227, no. 6, pp. 3058–3088, 2008.
- [20] D. P. Brown, E. I. Kauppinen, J. K. Jokiniemi, S. G. Rubin, and P. Biswas, "A method of moments based CFD model for polydisperse aerosol flows with strong interphase mass and heat transfer," *Comput. Fluids*, vol. 35, no. 7, pp. 762–780, 2006.
- [21] S. Subramaniam, "Lagrangian-Eulerian methods for multiphase flows," *Prog. Energy Combust. Sci.*, vol. 39, pp. 215–245, 2013.
- [22] D. Kang and R. K. Strand, "Modeling of simultaneous heat and mass transfer within passive down-draft evaporative cooling (PDEC) towers with spray in FLUENT," *Energy Build.*, vol. 62, pp. 196–209, 2013.
- [23] V. Kalantar, "Numerical simulation of cooling performance of wind tower (Baud-Geer) in hot and Arid region," *Renewable Energy*, vol. 34, pp. 246–254, 2009.
- [24] M. J. Cook, D. Robinson, K. J. Lomas, N. T. Bowman, and H. Eppel, "Passive draught evaporative cooling: II. Airflow modelling," *Indoor Built Environ.*, vol. 9, pp. 325–334, 2000.
- [25] B. E. Launder and D. B. Spalding, "The numerical computation of turbulent flows," *Comput. Methods Appl. Mech. Eng.*, vol. 3, pp. 269–289, 1974.
- [26] ANSYS FLUENT 14.5: Theory Guide, ANSYS Inc.
- [27] S. A. Morsi and A. J. Alexander, "An investigation of particle trajectories in two-phase flow systems," *J. Fluid Mech.*, vol. 55, no. 2, pp. 193–208, 1972.
- [28] R. S. Miller, K. Harstad, and J. Bellan, "Evaluation of equilibrium and non-equilibrium evaporation models for many droplet gas-liquid flow simulations," *Int. J. Multiphase Flow*, vol. 24, no. 6, pp. 1025–1055, 1998.
- [29] S. S. Sazhin, "Advanced models of fuel droplet heating and evaporation," *Prog. Energy Combust. Sci.*, Elsevier Science, vol. 32, pp. 162–214, 2006.
- [30] W. E. Ranz and W. R. Marshall, Jr., "Evaporation from drops, part I," *Chem. Eng. Prog.*, vol. 48, no. 3, pp. 141–146, 1952.
- [31] W. E. Ranz and W. R. Marshall, Jr., "Evaporation from drops, part I and part II," *Chem. Eng. Prog.*, vol. 48, no. 4, pp. 173–180, 1952.
- [32] S. V. Patankar, *Numerical Heat Transfer and Fluid Flow*. New York, NY: Hemisphere Publishing, 1980.
- [33] F. Moukalled, L. Mangani, and M. Darwish, *The Finite Volume Method in Computational Fluid Dynamics: An Advanced Introduction with OpenFOAM® and Matlab®*. Switzerland: Springer, 2015.

- [34] I. Demirdzic, "On the discretization of the diffusion term in finite-volume continuum mechanics," *Numer. Heat Transfer, Part B*, vol. 68, no. 1, pp. 1–10, 2015.
- [35] M. Darwish and F. Moukalled, "A compact procedure for discretization of the anisotropic diffusion operator," *Numer. Heat Transfer, Part B*, vol. 55, no. 5, pp. 339–360, 2009.
- [36] S. G. Rubin and P. K. Khosla, "Polynomial interpolation method for viscous flow calculations," *J. Comput. Phys.*, vol. 27, pp. 153–168, 1982.
- [37] C. M. Rhie and W. L. Chow, "Numerical study of the turbulent flow past an airfoil with trailing edge separation," *AIAA J.*, vol. 21, p. 1525, 1983.
- [38] S. V. Patankar and D. B. Spalding, "A calculation procedure for heat, mass and momentum transfer in three-dimensional parabolic flows," *Int. J. Heat Mass Transfer*, vol. 15, pp. 1787–1806, 1972.
- [39] ASHRAE, *ASHRAE Fundamentals Handbook (SI)*, American Society of Heating, Refrigerating and Air Conditioning Engineers, chapter 6, 2001.
- [40] R. Belarbi, C. Ghiaus, and F. Allard, "Modeling of water spray evaporation: Application to passive cooling of buildings," *Sol. Energy*, vol. 80, pp. 1540–1552, 2006.
- [41] M. Ragheb and A. M. Ragheb, "Wind turbines theory - The Betz equation and optimal rotor tip speed ratio," in *Fundamental and Advanced Topics in Wind Power*, R. Carriveau, Ed. Croatia: InTech Publisher, 2011, pp. 19–38.
- [42] D. Zaslavsky, U. Wurzburger, A. Einav, and S. Setty, "Energy towers for producing electricity and desalinated water without a collector," 2001. Available http://www.transnational-renewables.org/Gregor_Czisch/projekte/new_et-brochure_zaslavsky.pdf